optica

Three-dimensional band diagram in lateral polarity junction III-nitride heterostructures

Wei Guo,[1,2] Somak Mitra,[3] Jie'an Jiang,[1,4,5] Houqiang Xu,[1,4] Moheb Sheikhi,[1,4] Haiding Sun,[2] Kangkai Tian,[6] Zi-hui Zhang,[6] Haibo Jiang,[7] Iman S. Roqan,[3] Xiaohang Li,[2,8] and Jichun Ye[1,4,9]

[1]Ningbo Institute of Materials Technology and Engineering, Chinese Academy of Sciences, Ningbo 315201, Zhejiang, China
[2]Advanced Semiconductor Laboratory, King Abdullah University of Science and Technology (KAUST), Thuwal 23955, Saudi Arabia
[3]Physical Science and Engineering Division, King Abdullah University of Science and Technology (KAUST), Thuwal 23955, Saudi Arabia
[4]University of Chinese Academy of Sciences, Beijing 100049, China
[5]ShanghaiTech University, Pudong, Shanghai 201210, China
[6]Hebei University of Technology, Institute of Micro-Nano Photoelectron and Electromagnetic Technology Innovation, School of Electronics and Information Engineering, Tianjin 300401, China
[7]School of Molecular Sciences, University of Western Australia, Perth 6009, Australia
[8]e-mail: xiaohang.li@kaust.edu.sa
[9]e-mail: jichun.ye@nimte.ac.cn

Received 3 January 2019; revised 14 July 2019; accepted 15 July 2019 (Doc. ID 356344); published 13 August 2019

The 2D band diagram comprising out-of-plane potentials has been ubiquitously utilized for III-nitride heterostructures. Here, we propose the 3D band diagram based on unambiguous evidences in luminescence and carrier dynamics for lateral polarity junction quantum wells: although electrons and holes are separated out-of-plane in quantum wells by polarization, different band diagram heights lead to secondary carrier injection in-plane, causing electrons to transport from the III- to N-polar domains to recombine with holes therein with large wavefunction overlap. We also show that utilization of the 3D band diagram can be extended to single-polarity structures to analyze carrier transport and dynamics, providing new dimensions for accurate optical device design. © 2019 Optical Society of America under the terms of the OSA Open Access Publishing Agreement

https://doi.org/10.1364/OPTICA.6.001058

1. INTRODUCTION

III-nitride semiconductors have enabled numerous essential optical applications including lighting and display. For III-nitrides, one of the most interesting properties is the lattice polarity. The polarity can be III- or N-polar with the opposite spontaneous polarization, and piezoelectric polarization occurs under strain [1,2]. Numerous studies have explored the polarizations for optical devices including UV to infrared light-emitting diodes (LEDs) and lasers [3,4]. Thus far, virtually all reported III-nitride heterostructures and devices are of single polarity, i.e., either III- or N-polar. The III-polarity is commonly employed to obtain sharp interface and high crystal quality, albeit researchers have demonstrated high quality N-polar materials and devices including decent p-type doping of AlGaN for LEDs [5,6].

The design and optimization of most III-nitride devices hinge on device band diagrams to accurately compute and analyze carrier transport and dynamics processes including recombination. Conventionally, for single-polarity optical devices, the 2D band diagram comprising out-of-plane potentials of conduction and valence bands has been ubiquitously utilized [7]. For instance, in III- or N-polar quantum wells (QWs), what injected carriers see is a 2D lower-potential slab sandwiched by two higher-potential quantum barriers (QBs), forming the out-of-plane QW/QB heterojunction. Hence, the 2D band diagram has been utilized to describe carrier phenomena including the quantum confined Stark effect (QCSE) where electron and hole wavefunctions are spatially separated out-of-plane by the polarizations, thereby leading to reduced radiative recombination efficiency [7].

Recently, the lateral polarity junction (LPJ) has been demonstrated [8–10]. Not only III- and N-polar regions can be grown side by side simultaneously on the same wafer forming in-plane homojunction, but also out-of-plane heterojunctions can be formed along the growth direction [8]. We show that by reducing the LPJ to micrometer size, emission intensity of the LPJ multiple QWs (MQWs) can be dramatically improved compared to the uniform III-polar MQWs [8]. However, it is unclear exactly how the LPJ enhances radiative recombination. Also, the combination of vertical heterojunctions and lateral homojunctions inevitably leads to more complex carrier transport and dynamics.

In this work, carrier transport and dynamics, as well as the recombination process of the LPJ MQWs are investigated and analyzed. Based on unambiguous luminescent and carrier lifetime evidences, we hypothesize that the LPJ can enable the secondary carrier injection such that electrons transport laterally in the QW due to the in-plane potential difference of band diagrams, thereby suppressing the QCSE. Different from the conventional 2D band diagram model, we propose the 3D band diagram model to explain carrier transport

and dynamics of the LPJ MQWs. Additionally, we point out that the applications of the 3D band diagram can be further extended to single-polarity structures with in-plane potential variation and out-of-plane band bending. Therefore, the proposal of the 3D band diagram could inspire new perspectives in the design and analysis of III-nitride optical devices regardless of the polarity.

2. EXPERIMENT

The epitaxial thin-film structure comprises a 1-μm AlN/sapphire template, a 400-nm composition-graded $Al_xGa_{1-x}N$ layer, a 600-nm $Al_{0.2}Ga_{0.8}N$ layer, and 10 pairs of 5-nm $Al_{0.1}Ga_{0.9}N$/3 nm GaN MQWs along the *c*-axis. The epitaxial and fabrication processes are similar to a previous study where the uniformly distributed circular pattern is the III-polar domain and the matrix is the N-polar domain [8]. The center-to-center distance between two neighboring circular patterns is 6 μm. For comparison, two additional samples of uniform III- and N-polar MQWs without any pattern were grown with the same structure and condition. Cathodoluminescence (CL) investigations were carried at RT with electron voltage of 5 kV and 188 μA. Spatially resolved photoluminescence (PL) was characterized using a 325-nm laser at RT. Time-resolved PL (TRPL) experiments were performed with a mode-locked Ti:sapphire laser at RT and 5 K. The beam diameter of the TRPL laser was ~60 μm, thereby covering tens of the III-polar domains along with surrounding N-polar domains when probing the LPJ MQWs.

3. RESULTS AND DISCUSSION

Figure 1(a) represents the spatially resolved PL intensity at the peak wavelength of 353 nm of the grown LPJ MQWs at RT. Apparently, the PL intensities in the N-polar domains are much higher than that of the III-polar domains. In Fig. 1(a), we randomly pick up 10 individual spectra from both III- and N-polar domains. The overall intensities are four to six times higher in the N-polar domains than those in the III-polar domains shown in Fig. 1(b), consistent with our previous study where the measurement of the relative internal quantum efficiency can be found [8]. The peak positions of the 10 spectra in Fig. 1(b) are summarized in Table 1. The average peak position of the III-polar domain is 353.3 nm, whereas that of the N-polar domain is 355.1 nm. The 1.8-nm red shift could be negligible, given the variation of the peak positions among the spectra of III- or N-polar domains is comparable.

To further understand sub-microscale optical behavior of the LPJ MQWs, CL spectra were recorded at RT. In Fig. 2(a), the spectrum of the LPJ MQWs identifies two main peaks: one is located at ~343 nm consistent with the PL (Fig. 1) attributed to the

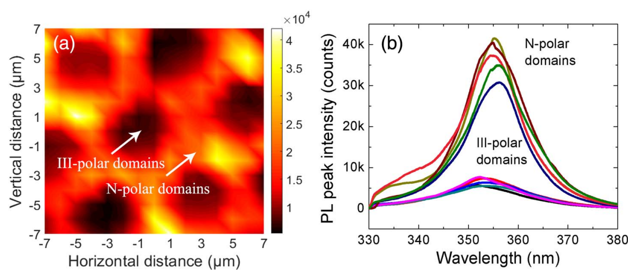

Fig. 1. (a) Spatial mapping of PL intensities at 353 nm of the LPJ MQW. (b) 10 spectra randomly picked from III- and N-polar domains in (a).

Table 1. Spectral Peaks in III- and N-Polar Domains

	Peaks (nm)	Avg. (nm)
III-Polar	352.5, 353.7, 353.9, 353.9, 352.5	353.3
N-Polar	355.3, 355.5, 354.7, 354.3, 355.7	355.1

MQW emission; and the broad peak is related to deep levels such as donor–acceptor pair or transition from conduction band to deep acceptors [11]. The shorter wavelength of the CL MQW peak compared to that of the PL peak may be attributed to the band filling effect due to much higher excitation electron energy amid CL experiments. Figures 2(b) and 2(c) show the CL emission from the LPJ MQWs (343 nm) and deep levels (449 nm). Clearly, the N-polar domains show much stronger MQW emission than the III-polar domains, which is consistent with the PL (Fig. 1). Figure 2(b) also manifests that the intensity enhancement is obviously limited within the border of the circular patterns, i.e., within the N-polar domains. The deep-level emission intensity of the III-polar domains is similar to that of the N-polar domains. Also, Fig. 2(b) exhibits localized MQW emission within the N-polar domains. To confirm, CL mapping from the N- and III-polar MQW samples was performed at 343 nm [Figs. 2(d) and 2(e)]. The latter shows homogeneous emission while the former exhibits localized emission in good agreement with Fig. 2(b), which could be related to surface roughness [8,12].

The introduction of the LPJ to the out-of-plane heterojunction MQWs apparently adds to in-plane complexity of carrier transport and dynamics. One consequence is that the N-polar domains exhibited much stronger PL and CL than the III-polar ones. To understand the behavior, carrier dynamics of the LPJ MQW sample, and the III- and N-polar MQW samples were investigated by TRPL at 5 K. Figure 3(a) shows that the decays can be characterized by bi-exponential decay:

$$I(t) = A_f \exp\left(-\frac{t}{\tau_f}\right) + A_s \exp\left(-\frac{t}{\tau_s}\right). \quad (1)$$

A_f and A_s are fast and slow peak intensities before decaying. τ_f and τ_s are decay lifetimes of the fast and slow components summarized in Table 2. It is assumed that non-radiative recombination centers froze up at 5 K. Therefore, both τ_f and τ_s are representative of the radiative recombination processes [13]. Both τ_f and τ_s are significantly shorter for the LPJ MQWs than

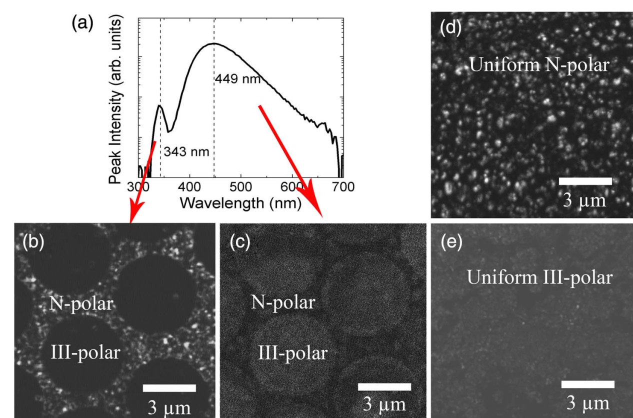

Fig. 2. (a) CL spectrum of the LPJ MQWs with monotonic CL intensity distribution collected at (b) $\lambda = 343$ nm and (c) $\lambda = 449$ nm. Monotonic CL intensity distribution of (d) the N-polar MQW sample and (e) the III-polar MQW sample collected at $\lambda = 343$ nm.

Table 2. Decay Lifetimes at 5 K [Fig. 3(a)]

	τ_f (ns)	τ_s (ns)
III-polar MQWs	1.02	2.63
N-polar MQWs	1.25	3.71
LPJ MQWs	0.27	1.11

for the III- and N-polar MQWs, suggesting that the existence of the LPJ enables significantly more efficient radiative recombination for the LPJ MQWs as a whole. The τ_f and τ_s of the III-polar MQWs are moderately shorter than those of the N-polar MQWs. To further understand the carrier dynamics of the LPJ MQWs, PL decay curves were compared at 5 K and RT for the LPJ MQWs [Fig. 3(b)]. Both τ_f and τ_s of the LPJ MQWs at 5 K are considerably longer than those measured at RT which suggests that the non-radiative recombination plays a more significant role at RT, similar to conventional single-polarity samples [13].

The results of TRPL, CL, and PL experiments are remarkably interesting. The carrier lifetimes at 5 K show that the radiative recombination efficiency of the N-polar MQW sample is similar to, if not slightly worse than, that of the III-polar MQW sample. However, the PL and CL results show the N-polar domains of the LPJ MQWs emit dramatically higher intensity than the III-polar domains (Figs. 1 and 2). In addition, the carrier lifetimes at 5 K indicate the radiative recombination efficiency of the LPJ MQWs is significantly larger than the III- and N-polar MQW samples. These phenomena can be attributed only to LPJ's unique in-plane band profiles that could not be corroborated by the 2D band diagram conventionally employed for single-polarity structures.

Thereby, we propose the 3D band diagram to explain the phenomena that combines the out-of-plane heterojunction and the in-plane LPJ in Fig. 4. It is noted that the directions of band bending in the MQWs are opposite between III- and N-polar MQWs. Because the carrier wavefunctions centered around the potential minimum, specifically, electron wavefunctions are near positions A and F; and hole wavefunctions are near positions C and H. The external pumping results in the *primary* carrier injection into the MQWs at both III- and N-domains. Afterwards, we hypothesize that the *secondary* carrier injection process happens: electrons near the potential minimum of the conduction band in the III-polar domains (position A) can transport laterally to that of the N-polar domains (position E) on the same *c*-plane due to lower potentials of the band diagrams of the N-polar domains. Consequently, those electrons can recombine radiatively with holes located near position H at the same physical position, i.e., with high wavelength function overlap and thus significantly enhanced emission. We believe the secondary carrier

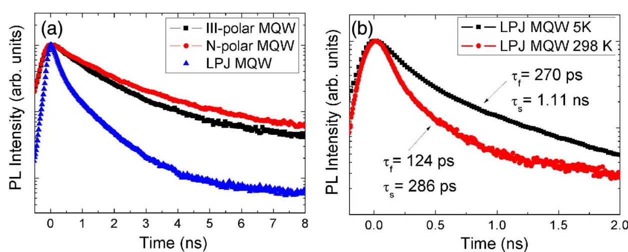

Fig. 3. TRPL spectra of (a) the LPJ MQW, III-polar MQW, and N-polar MQW samples at 5 K and (b) the LPJ MQW sample at 5 K and RT.

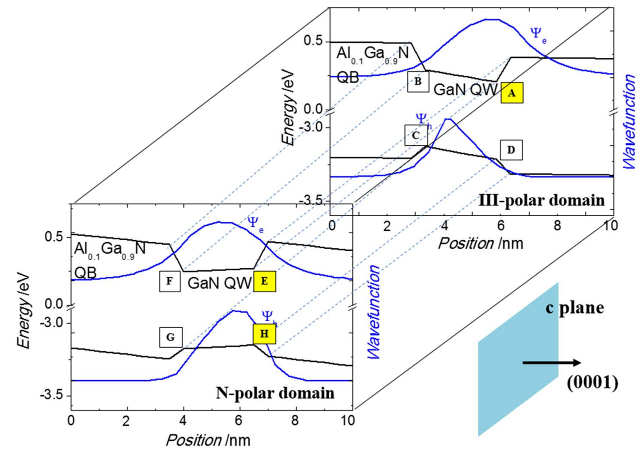

Fig. 4. 3D band diagram of the LPJ MQWs comprising two 2D band diagrams, one for the N-polar domain and the other for the III-polar domain. Carrier ground state wavefunctions are included for the two 2D band diagrams by solving the Poisson equations and carrier transport equations. Dashed lines represent the in-plane interface between the N- and III-polar domains, connecting the band edges of III- and N-polar domains laterally on the same *c*-plane. Positions A and D, B and C, E and H, F and G are in the same physical position, respectively.

injection is dominated mainly by electrons due to much smaller mobility of holes. Also, there should not be much secondary carrier injection from the N- to III-polar domains supported by the well-defined border of the much stronger MQW CL in the N-polar domains than the III-polar domains [Fig. 2(b)]. Some may point out that electrons may transport from position A and/or position E to lower-potential position F of the N-polar domains. We agree, but we do not view it as the dominant process, because the overwhelming hole existence near position H (the same physical location as position E) can lead to much faster radiative recombination [Fig. 3(a)] and provide electrostatic attraction to mitigate the electron transport to position F.

Previously, Fiorentini proposed a lateral potential model to explain the enhanced PL in the vicinity of the GaN LPJ [14]: an electron potential maximum sandwiched by two electron potential minima on the scale of around 5 Å is at the boundary of the LPJ. Thus, electrons are captured in the two potential minima while holes are trapped in the electron potential maximum, which is followed by radiative recombination. Considering that the lateral dimension of the electron and hole trapping area is only a few Å in Fiorentini's model, the enhanced PL should be observed within the similar dimension of the area, which is in stark contrast to observations by Stutzmann, Kirste, and us, including this study, that the areas of enhanced PL are at least several micrometers wide [8–10]. Also, Fiorentini's model indicates that both sides of the LPJ trap electrons and thus both sides should have enhanced PL. However in Fig. 2(b), the enhancement occurs only within the circular N-polar domains even under high-energy e-beam pumping, which evidently indicates the secondary carrier injection is mainly one-way, i.e., from the III- to N-polar domains amid the 3D band diagram.

The in-plane secondary carrier injection directly led to two outcomes. First, it causes much stronger radiative recombination in the N-polar domains reflected by PL and CL [Figs. 1 and 2(b)]. Second, the *extrinsic* electron–hole wavefunction overlap between positions E and H in the N-polar domains is much greater than (i) the *intrinsic* wavefunction overlap between positions A and C

(III-polar domains), and (ii) the intrinsic wavefunction overlap between positions F and H (N-polar domains). As a result, the QCSE is greatly reduced, leading to significantly shorter radiative carrier lifetime in the LPJ MQWs as a whole than those of III- and N-polar MQWs. We note that the proposed 3D band diagram and associated secondary injection apply not only to this study but also other LPJ structures with in-plane carrier transport.

4. EXTENSIONS OF 3D BAND DIAGRAM

We would like to point out that the proposed 3D band diagram can also apply for the single-polarity structures for optical devices typically depicted by the 2D band diagram, because there could be considerable in-plane and out-of-plane potential variations due to current crowding, which could greatly hinder device performance. As an example, we hereby present the analysis of a simplified mesa-structure III-polar LED. A 3-nm GaN single QW (SQW) followed by a 20-nm $Al_{0.2}Ga_{0.8}N$ electron blocking layer (EBL) is sandwiched by 3.5-μm $n-Al_{0.1}Ga_{0.9}N$ and 500-nm $p-Al_{0.1}Ga_{0.9}N$ cladding layers with Si and Mg doping concentrations of 5×10^{18} and 1×10^{19} cm^{-3}. The mesa length and height are 180 and 2 μm, respectively [Fig. 5(a)]. The mesa width is 500 μm (perpendicular to the screen). The applied bias between *p*- and *n*-electrodes is 5 V resulting in device current of 160 mA and thus average mesa current density of 178 A/cm^2. The inset in Fig. 5(a) shows current crowding near the edge close to the n-electrode. Figure 5(a) manifests that lateral electron and hole concentrations in the middle of the GaN SQW reach maximum at $x = 175$ μm and decrease rapidly when x is away from 175 μm, indicating significant inhomogeneity and consistent with current crowding. Hence, electrons and holes can diffuse from $x = 175$ μm. Amid current crowding, the common out-of-plane 2D band diagrams at different x values could vary considerably in two aspects: potential height and band bending. Figure 5(b) shows the out-of-plane 2D band diagrams at the SQW at $x = 90$ and 170 μm from two dashed lines A and B in Fig. 5(c), respectively. It is apparent that the band diagram of both conduction and valence bands at $x = 170$ μm are higher by ~0.26 eV than that at $x = 90$ μm. This indicates that there would be lateral electron drift from $x = 170$ to 90 μm, and vice versa for hole drift. Moreover, due to carrier screening of polarization, band bending of the SQW becomes weaker at $x = 170$ μm, confirmed by improved overlap between ground-state electron and hole wavefunctions from 23% to 28% and blue-shifted transition energy from 3.461 eV to 3.473 eV from $x = 90$ to 170 μm, i.e., weaker QCSE. Furthermore, conduction band potentials from $x = 0$ to 180 μm near the SQW are plotted in Fig. 5(c), exhibiting significant inhomogeneity with variations from 3.21 eV to 3.80 eV within the SQW.

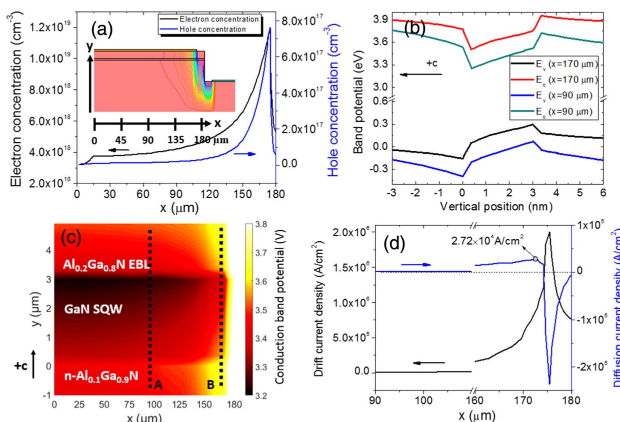

Fig. 5. (a) Lateral carrier concentrations in the middle of the 3-nm SQW [$y = 1.5$ nm in (c)]. The inset shows the mesa with current density contour; (b) 2D band diagrams at the SQW at $x = 90$ and 170 μm along black dashed lines A and B in (c); (c) conduction band potentials near the SQW; (d) lateral diffusion and drift current densities at $y = 1.5$ nm.

Due to the differences in carrier concentrations and band potentials, the lateral carrier diffusion and drift are expected. Using electrons for instance, lateral diffusion and drift current densities are represented by Eqs. (2) and (3):

$$J^{\text{lateral}}_{\text{diffusion}} = -qD\frac{dn}{dx}, \tag{2}$$

$$J^{\text{lateral}}_{\text{drift}} = qn\mu E = qn\mu\frac{dV}{dx}. \tag{3}$$

q is unit charge, D is diffusion coefficient, n is concentration, μ is mobility, E is electric field, and V is conduction band potential. $D = \mu\frac{kT}{q}$ where $\mu = 2000$ cm^2/Vs at RT [15]. Figure 5(d) shows the lateral drift and diffusion current densities in the middle of the SQW based on Figs. 5(a) and 5(c). The largest diffusion and drift current densities are -2.4×10^5 and 1.8×10^6 A/cm^2 at $x = 175$ μm, corresponding to the greatest gradients of electron concentration and conduction band potential versus the lateral position. Thus, the net lateral current density of 1.56×10^6 A/cm^2 is four orders of magnitude greater than the average mesa current density. This clearly illustrates that there is strong secondary carrier injection laterally to compensate the gradients, which could greatly affect carrier dynamics and recombination, and possibly junction temperatures. Away from $x = 175$ μm, the lateral current densities gradually reduce. Because of the inhomogeneous in-plane potentials and varying band bending, the 3D diagram similar to Fig. 5 can be plotted between two lateral positions from 0 μm to 180 μm comprising two 2D band diagrams laterally connected by a plurality of 2D band diagrams with varying in-plane potentials and out-of-plane band bending in between. Subsequently, lateral carrier transport and dynamics including recombination can be analyzed to facilitate high-accuracy optical device design. For III-nitride electronic, especially power electronic devices, it is important to note that the in-plane design has been utilized extensively for field management and carrier injection control, since issues such as electric breakdown and channel current are closely related to the in-plane electric field gradient [16,17].

5. CONCLUSION

We proposed the 3D band diagram comprising two out-of-plane 2D band diagrams based on unambiguous evidences from PL, CL, and TRPL experiments of the LPJ MQWs. Amid the 3D band diagram, electrons of the III-polar domains can laterally transport to the N-polar domains due to different in-plane band diagram heights to recombine with holes therein with large wavefunction overlap, greatly reducing radiative carrier lifetimes and enhancing luminescence. More broadly, the applications of the 3D band diagram can be extended to single-polarity structures such as III-polar LEDs due to current crowding causing in-plane potential variation and out-of-plane band bending change. The

resulting in-plane diffusion and drift current densities can be several orders of magnitude larger than the out-of-plane average mesa current density. This study provides new perspectives and degrees of freedom in highly accurate design and analysis of III-nitride optical devices of single polarity and with the LPJ.

Funding. National Key Research and Development Program of China (2016YFB0400802); National Natural Science Foundation of China (NSFC) (61574145, 61704176); Natural Science Foundation of Zhejiang Province (LY15F040003); KAUST Baseline (BAS/1/1664-01-01); KAUST CRG (URF/1/3437-01-01, URF/1/3771-01-01); KAUST GCC (REP/1/3189-01-01).

REFERENCES

1. F. Bernardini, V. Fiorentini, and D. Vanderbilt, "Spontaneous polarization and piezoelectric constants of III-V nitrides," Phys. Rev. B **56**, R10024 (1997).
2. C. E. Dreyer, A. Janotti, C. G. Van de Walle, and D. Vanderbilt, "Correct implementation of polarization constants in wurtzite materials and impact on III-nitrides," Phys. Rev. X **6**, 021038 (2016).
3. J. Simon, V. Protasenko, C. Lian, H. Xing, and D. Jena, "Polarization-induced hole doping in wide–band-gap uniaxial semiconductor heterostructures," Science **327**, 60–64 (2010).
4. Y. Sun, K. Zhou, Q. Sun, J. Liu, M. Feng, Z. Li, Y. Zhou, L. Zhang, D. Li, and S. Zhang, "Room-temperature continuous-wave electrically injected InGaN-based laser directly grown on Si," Nat. Photonics **10**, 595 (2016).
5. S. Keller, N. Fichtenbaum, F. Wu, D. Brown, A. Rosales, S. DenBaars, J. Speckand, and U. Mishra, "Influence of the substrate misorientation on the properties of N-polar GaN films grown by metal organic chemical vapor deposition," J. Appl. Phys. **102**, 083546 (2007).
6. L. Yan, Y. Zhang, X. Han, G. Deng, P. Li, Y. Yu, L. Chen, X. Li, and J. Song, "Polarization-induced hole doping in N-polar III-nitride LED grown by metalorganic chemical vapor deposition," Appl. Phys. Lett. **112**, 182104 (2018).
7. F. Wu, H. Sun, I. A. Ajia, I. S. Roqan, D. Zhang, J. Dai, C. Chen, Z. C. Feng, and X. Li, "Significant internal quantum efficiency enhancement of GaN/AlGaN multiple quantum wells emitting at ~350 nm via step quantum well structure design," J. Phys. D **50**, 245101 (2017).
8. W. Guo, H. Sun, B. Torre, J. Li, M. Sheikhi, J. Jiang, H. Li, S. Guo, K.-H. Li, A. Giugni, E. D. Fabrizio, X. Li, and J. Ye, "Lateral-polarity structure of AlGaN quantum wells: a promising approach to enhancing the ultraviolet luminescence," Adv. Funct. Mater. **28**, 1802395 (2018).
9. M. Stutzmann, O. Ambacher, M. Eickhoff, U. Karrer, A. Lima Pimenta, R. Neuberger, J. Schalwig, R. Dimitrov, P. Schuck, and R. Grober, "Playing with polarity," Phys. Status Solidi B **228**, 505–512 (2001).
10. R. Kirste, R. Collazo, G. Callsen, M. R. Wagner, T. Kure, J. S. Reparaz, S. Mita, J. Xie, A. Rice, and J. Tweedie, "Temperature dependent photoluminescence of lateral polarity junctions of metal organic chemical vapor deposition grown GaN," J. Appl. Phys. **110**, 093503 (2011).
11. Y. Isobe, H. Hung, K. Oasa, T. Ono, T. Onizawa, A. Yoshioka, Y. Takada, Y. Saito, N. Sugiyama, and K. Tsuda, "Defect analysis in GaN films of HEMT structure by cross-sectional cathodoluminescence," J. Appl. Phys. **121**, 235703 (2017).
12. M. Hou, Z. Qin, L. Zhang, T. Han, M. Wang, F. Xu, X. Wang, T. Yu, Z. Fang, and B. Shen, "Excitonic localization at macrostep edges in AlGaN/AlGaN multiple quantum wells," Superlattices Microstruct. **104**, 397–401 (2017).
13. I. A. Ajia, P. R. Edwards, Y. Pak, E. Belekov, M. A. Roldan, N. Wei, Z. Liu, R. W. Martin, and I. S. Roqan, "Generated carrier dynamics in V-pit-enhanced InGaN/GaN light-emitting diode," ACS Photon. **5**, 820 (2017).
14. V. Fiorentini, "Origin of the efficient light emission from inversion domain boundaries in GaN," Appl. Phys. Lett. **82**, 1182–1184 (2003).
15. J.-T. Chen, I. Persson, D. Nilsson, C.-W. Hsu, J. Palisaitis, U. Forsberg, P. O. Persson, and E. Janzén, "Room-temperature mobility above 2200 cm2/V· s of two-dimensional electron gas in a sharp-interface AlGaN/GaN heterostructure," Appl. Phys. Lett. **106**, 251601 (2015).
16. H. Amano, Y. Baines, E. Beam, M. Borga, T. Bouchet, P. R. Chalker, M. Charles, K. J. Chen, N. Chowdhury, and R. Chu, "The 2018 GaN power electronics roadmap," J. Phys. D **51**, 163001 (2018).
17. S. Yoshida, H. Ishii, J. Li, D. Wang, and M. Ichikawa, "A highpower AlGaN/GaN heterojunction field-effect transistor," Solid-State Electron. **47**, 589–592 (2003).